

Single NV Centers as Sensors for Radio-Frequency Fields

Jingfu Zhang and Dieter Suter
Fakultaet Physik, Technische Universitaet Dortmund,
D-44221 Dortmund, Germany
(Dated: July 13, 2022)

We show that a single electron spin can serve as a sensor for radio-frequency (RF) magnetic fields. The longitudinal and transverse components of the RF field can be extracted from the phase acquired during free evolution of the spin coherence. In our experimental demonstration, a single electron spin of an NV center in diamond serves as an atomic-size of two components of an RF field.

PACS numbers: 03.65.Ta, 07.55.Ge, 76.30.Mi

Introduction.—Quantum sensing can be defined as the use of the quantum properties of a probing system (sensor) for measuring physical quantities, such as temperature, time, electric and magnetic fields [1]. Quantum systems that can be used as sensors include ensembles of nuclear spins [2], atomic vapors [3, 4], trapped ions [5, 6], Rydberg atoms [7], superconducting circuits (e.g. SQUIDS) [8–10] and nitrogen-vacancy (NV) centers in diamond, either in the form of ensembles or single spins [11–14].

Over the last years, it became evident that developments in different quantum technologies can generate useful synergies. As an example, progress in quantum sensing can be supported by algorithms and concepts developed for quantum information, where the quantum bits (qubits) are used for processing information [15, 16]. The information content of a quantum state is the essential property for optimal performance and can be used to determine fundamental limits to the sensitivity of a specific sensing modality [17]. In both fields, the information must be protected against unwanted environmental noise [18], while the interactions with the environment can be tailored such that the sensor extracts the targeted information but rejects unwanted perturbations [19]. Techniques like dynamical decoupling (DD) [20–23] or quantum error correction [18, 24, 25] and extended quantum memories [20, 26–30] can enhance the sensitivity of quantum sensing.

Here we focus on using single electron spins from NV centers in diamond [13] as quantum sensors for oscillating magnetic fields i.e., AC fields. The main advantages of the NV centers for quantum sensing include high sensitivity, precision and spatial resolution down to atomic scale [31]. These beneficial properties are associated with the strong interaction between the electron spin and magnetic fields. Powerfull control operations have been developed for this sensor, using resonant microwave fields and optical excitation. Readout is accomplished through efficient single-photon counting techniques. NV centers have been used as quantum sensors in biological systems, to provide access and insight into the structure and function of individual biomolecules and observe biological processes at the quantum level with atomic resolution [32].

NV centers can perform as sensors for both DC and

AC magnetometry, with one or multiple centers, e.g., based on Rabi oscillation or spin-locking [1, 11, 33–40]. Most previous works on AC magnetometry were based on pulsed DD or continuous driving techniques such as spin-locking [11, 33]. However, with this approach, the frequency or the strength of the AC field that can be detected is limited by the Rabi frequencies of the DD pulses, and the continuous microwave (MW) driving or too many DD pulses might cause undesired effects, such as MW broadening. Moreover, these techniques are only sensitive to DC fields or to AC fields in a very narrow frequency range.

In this Letter, we propose and experimentally demonstrate a different strategy that does not suffer from these limitations: we encode the longitudinal and the transverse terms of an AC magnetic field in the phase of a coherent superposition of different spin states, where the MW fields are used only to generate and detect the coherence and therefore do not put any limitations to the fields to be measured. Moreover, in contrast to existing approaches, our scheme can detect multiple frequency components simultaneously. The experiments were performed at room temperature, using a diamond sample isotopically enriched in ^{12}C to 99.995% [41–43].

Theory.—The interaction between the electron spin and the RF field can be described by the Hamiltonian

$$\mathcal{H}_e(t) = (\omega_z S_z + \omega_x S_x) \sin(\omega_{RF} t + \varphi_0). \quad (1)$$

Here the amplitudes of the z - and x -component of the RF field are $\omega_z = -2\gamma_e B_{1,z}^{rf}$, $\omega_x = -2\gamma_e B_{1,x}^{rf}$ and φ_0 denotes the initial phase of the RF field. S_z and S_x denote the spin-1 operators for the electron. We use a coordinate system where the z -axis is oriented along the symmetry axis of the NV and the RF field lies in the xz -plane. The first term in Eq. (1) describes the longitudinal component of the RF field [44]. It commutes with the static system Hamiltonian and changes the energy levels and transition frequencies in first order. The second term couples to the transverse spin component S_x . It does not generate a first order shift, but the resulting second-order effect in the RF field amplitude, which is known as Bloch-Siegert shift (BSS) [45, 46], also contributes to a shift of the energy levels. Since the second-order effect also commutes with the static Hamiltonian, it can

be treated independently of the effect of the longitudinal term.

We start with the longitudinal term, which shifts the energy levels of the electron spin by $\delta\mathcal{E}_m = -\omega_z m \sin(\omega_{rf}t + \varphi_0)$, where m is the corresponding eigenvalue of S_z . A coherence between states $|m\rangle$, $|m'\rangle$ then acquires a phase

$$\begin{aligned}\varphi_z(\tau_p) &= -\omega_z(m - m') \int_0^{\tau_p} \sin(\omega_{rf}t + \varphi_0) dt \\ &= \alpha[\cos(\omega_{rf}\tau_p + \varphi_0) - \cos(\varphi_0)],\end{aligned}\quad (2)$$

where $\alpha = (m - m')\omega_z/\omega_{rf}$ and τ_p is the duration of the RF pulse.

The effects of the acquired phase can be observed using the pulse sequence shown in Fig. 1. The initial state of the electron spin is $|m\rangle$. The first $\pi/2$ pulse generates the superposition of states $|m\rangle$ and $|m'\rangle$. The second $\pi/2$ pulse converts part of the coherence to population, which can be read out. The resulting signal depends on φ_z as

$$P_{|0\rangle}(\tau_p) = [1 - \cos \varphi_z(\tau_p)]/2. \quad (3)$$

For spectral analysis, we write $\cos \varphi_z(\tau_p)$ as a Fourier series by using

$$\cos \varphi_z(\tau_p) = \cos(\alpha \cos \varphi_0) S_c + \sin(\alpha \cos \varphi_0) S_s. \quad (4)$$

Here $S_c \equiv \cos(\alpha \cos x)$, $S_s \equiv \sin(\alpha \cos x)$ are Fourier series:

$$\begin{aligned}S_c &= J_0(\alpha) + 2 \sum_{n=1}^{\infty} (-1)^n J_{2n}(\alpha) \cos(2nx) \\ S_s &= 2 \sum_{n=0}^{\infty} (-1)^n J_{2n+1}(\alpha) \cos[(2n+1)x]\end{aligned}\quad (5)$$

where $x = \omega_{rf}\tau_p + \varphi_0$ and $J_\nu(z)$ is the Bessel function of the first kind [47].

For the discussion of the second order effect (BSS), we consider a transition between two electron states with transition frequency Ω_0 . The BSS shifts this resonance frequency by

$$\omega_{BS} = \omega_x^2/(2\Omega_0). \quad (6)$$

The acquired phase of the coherence between states $|m\rangle$ and $|m'\rangle$ is

$$\varphi_x(\tau_p) = \omega_{BS}\tau_p. \quad (7)$$

The effects of the BSS can also be observed using the pulse sequence in Fig. 1. Eq. (3) becomes then

$$P_{|0\rangle}(\tau_p) = \{1 - \cos[\varphi_z(\tau_p) + \varphi_x(\tau_p)]\}/2. \quad (8)$$

Experimental demonstration for short signals.—We choose the electron states $|m_S = 0\rangle$ and $|m_S = -1\rangle$ for a quantitative study of these effects, starting with the first-order effect. We first initialize the electron into $|m_S = 0\rangle$ with

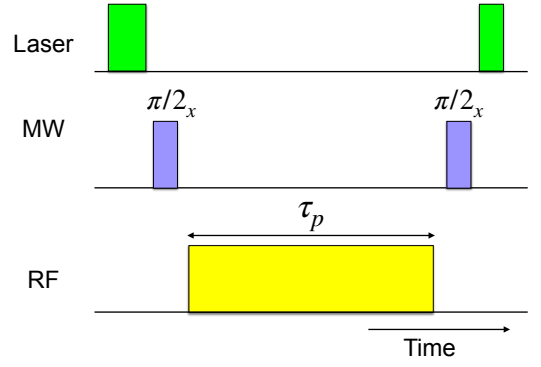


FIG. 1: Pulse sequence for sensing RF fields using the electron spin. The electron spin is initialized in state $|0\rangle$ by the first laser pulse. The first $\pi/2$ MW pulse generates the superposition of the spin states, and the second $\pi/2$ pulse converts one component of the coherence to population, which then can be read out by the second laser pulse.

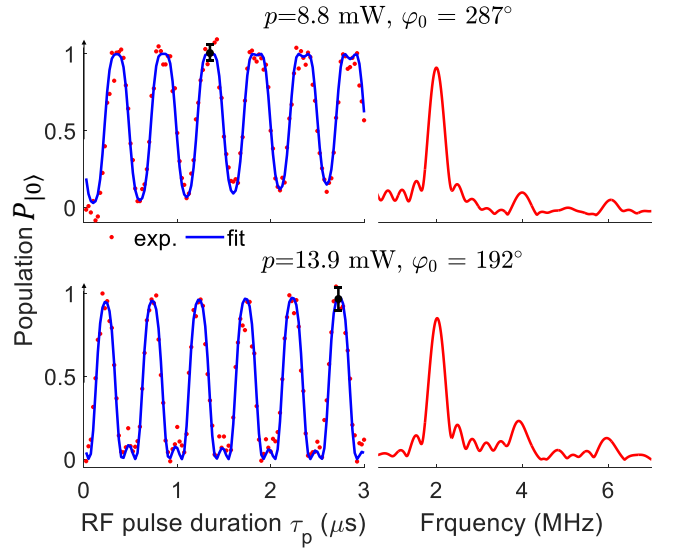


FIG. 2: Experimental results demonstrating the effect of the longitudinal component of the RF field on the electron spin at two different RF powers p of the RF pulses. The left column shows the population $P_{|0\rangle}$ as a function of the RF pulse duration τ_p . The error bars indicate the photon counting statistics. The dots represent the experimental data and the curves the fit to function (3), where the phase $\varphi_z(\tau_p)$ is given by Eq. (9). The right column shows the corresponding absolute value spectra.

the details given in section I of the supplementary material (SM). According to Eqs. (4-5), the first-order effect contributes components at frequencies $n\omega_{rf}$. We therefore record signals over a few periods $2\pi/\omega_{rf}$. On this timescale, dephasing effects are small (the dephasing time of the electron spin $T_2^* \approx 22 \mu\text{s}$, see section I of the SM). We use the pulse sequence shown in Fig. 1, with the RF frequency $\omega_{rf}/(2\pi) = 2 \text{ MHz}$ [48].

Fig. 2 shows the experimental results for two different

	$p = 8.8$	13.9 (mW)
$\omega_z/2\pi$ (MHz)	2.66 ± 0.02	3.24 ± 0.12
$\omega_x/2\pi$ (MHz)	35.2 ± 0.7	44 ± 1
$\omega_{DC}/2\pi$ (MHz)	-0.20 ± 0.01	-0.25 ± 0.01

TABLE I: Measured field amplitudes. $\omega_z/2\pi$ was obtained from the experimental data in Fig. 2, and $\omega_x/2\pi$ and $\omega_{DC}/2\pi$ from Fig. 5.

RF powers and initial phases φ_0 . The experimental time-domain signals (Fig. 2 left) show the expected periodicity in $2\pi/\omega_{rf} = 0.5 \mu\text{s}$. After several periods, the signal deviates from exact periodicity. These deviations are mostly due to the DC-component of the field and to the second-order effect, as discussed below. To include them in the fitting function, we modify $\varphi_z(\tau_p)$ in Eq. (2) to

$$\varphi_f(\tau_p) = \varphi_z(\tau_p) + (\omega_{DC} + \omega_{BS})\tau_p + \delta. \quad (9)$$

Here ω_{DC} is the projection of the DC component of the applied field to the z -axis and ω_{BS} the second-order contribution of the AC component, which generates a time-averaged frequency shift (see Eq. (6) and Ref. [45, 46]). ω_{DC} and ω_{BS} have different dependencies on the RF power level: ω_{DC} increases with the square root of the power and ω_{BS} increases quadratically with ω_x and thus linearly with the power. We can therefore separate the contributions by evaluating them at different power levels; details are given in the SM (section III E). The constant term δ appears to be due to transients generated by switching the RF pulse on and off with a finite rise time. The values for α , β and δ obtained by fitting the experimental data are listed in the SM (section III A). The field amplitudes ω_z at two different power levels are listed in Table I. The ratio between the two measured values of ω_z is 1.22, consistent with the ratio of the field strengths $\sqrt{13.9/8.8} = 1.26$.

The periodicity of these data suggests an analysis in the frequency domain. As shown in the Fourier transforms of the time domain data in Fig. 2, peaks appear at integer multiples of the RF frequency, $n\omega_{rf}$, in agreement with Eq. (4). Using the spectra in Fig. 2, we obtain the values of $\omega_z/2\pi$ consistent with the results obtained from the time-domain signals. The results are presented in the SM (section III B), together with additional details.

Measurement of the second order shift.—Since second order shifts are significantly smaller, measuring them requires higher precision and thus longer signals. Fig. 3 (a-b), shows some experimental results obtained with the pulse sequence in Fig. 1 and 8.8 mW RF power. The time domain signal can be fitted by

$$P_{|0\rangle}(\tau_p) = \{1 - e^{-\tau_p/T_2^*} \cos[\varphi_f(\tau_p)]\}/2, \quad (10)$$

where $T_2^* = 22 \mu\text{s}$, estimated from the FID measurement, see SM (section I).

To reduce noise-induced dephasing during these longer measurement periods, we use DD pulses [18, 21]. The

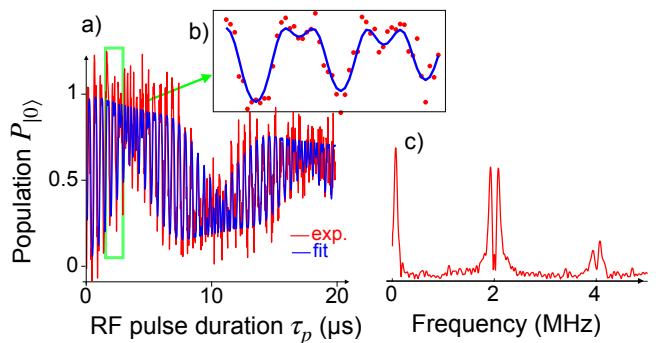


FIG. 3: Experimental results demonstrating first and second order contributions to the phase acquired by the electron spins by the pulse sequence shown in Fig. 1. (a) The population $P_{|0\rangle}$ as a function of the RF pulse duration τ_p . The red curve indicate the experiment data and the blue curves the fit by the function in Eq. (10). (b) Details for a short section, where the experimental data are indicated by filled circles. (c) Absolute value spectrum obtained from the experimental data in (a).

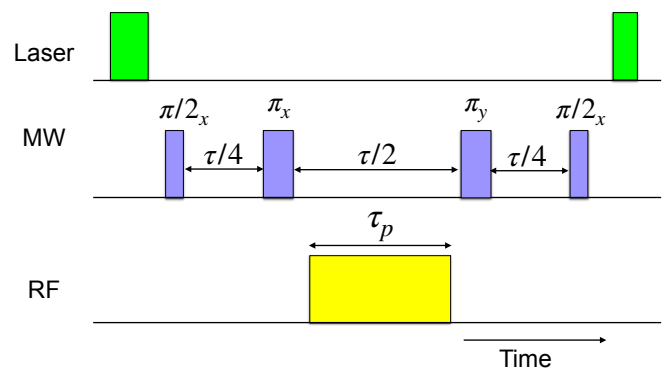


FIG. 4: Pulse sequence for sensing RF fields over longer time scales. The two π pulses are used to extend the coherence time of the electron spin. The other pulses are identical to those in Fig. 1.

pulse sequence shown in Fig. 4 includes two refocusing pulses with a $\pi/2$ phase shift for compensating cumulative pulse errors [49]. The phase generated by the RF pulse is not cancelled by the DD pulses, since the RF is applied only between the two refocusing pulses. The resulting phase is given by Eq. (9) and it is again transferred into measurable population by the final $\pi/2$ pulse, resulting in the signal

$$P_{|0\rangle}(\tau_p) = \{1 + \cos[\varphi_f(\tau_p)]\}/2. \quad (11)$$

Fig. 5(lhs) shows the measured signal $P_{|0\rangle}(\tau_p)$, for two different powers. Compared with the signal in Fig. 3 (a), the decay due to the dephasing effect is negligible, since the DD pulses extend the dephasing time up to 1.2 ms [46]. The fast oscillation (period $< 1 \mu\text{s}$) is due to the first order effect covered by the previous section, while the slower oscillation, whose period decreases drastically when the power level increases, is the topic of this section. The Fourier transforms of the time-domain data shown

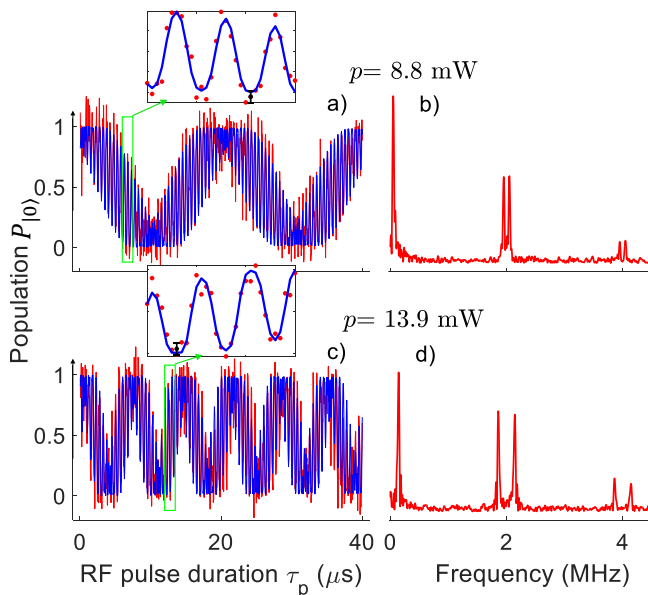


FIG. 5: Experimental results demonstrating first and second order contributions to the phase acquired by the electron spins at two different RF powers, using the pulse sequence shown in Fig. 4. The left column shows the population $P_{|0\rangle}$ as a function of the RF pulse duration τ_p . The red curves indicate the experimental data and the blue curves show the fit to function (11). The right column shows the absolute value spectra obtained from the experimental data on the left.

in Fig. 5 (rhs) contain peaks at the frequencies $|n\omega_{rf} \pm$

$(\omega_{DC} + \omega_{BS})/2\pi$, with $n = 0, 1$ and 2 . The values of the measured frequencies are listed in the SM(section IIIC). The calculated field amplitudes ω_{DC} and ω_x are listed in Table I, where Eq. (6) is used and Ω_0 is measured as 2.475151 GHz. These values agree with those obtained with the simpler pulse sequence in Fig. 1 (for details see SM(section IIIE)), but provide higher precision and accuracy. From the measured components ω_z and ω_x , we can estimate the angle θ between the NV axis and the RF field as $\theta \approx 86^\circ$.

Conclusion.—This work introduces a protocol for measuring time-dependent magnetic fields with a large frequency range, starting at zero. It can detect components parallel as well as perpendicular to the quantization axis with different sensitivity: the parallel (secular) component scales linearly with the amplitude of the field while the perpendicular component contributes in second order. Compared to methods based on spin-locking [33], our method is valid for weak and strong RF fields and covers a much larger frequency range. The experimental implementation is performed using the electron spin of an NV center in diamond. We consider a system where the field is magnetic, but it should be equally applicable to electric fields.

Acknowledgments.—This project has received funding from the European Union’s Horizon 2020 research and innovation programme under grant agreement No 828946. The publication reflects the opinion of the authors; the agency and the commission may not be held responsible for the information.

-
- [1] C. L. Degen, F. Reinhard, and P. Cappellaro, *Rev. Mod. Phys.* **89**, 035002 (2017).
- [2] N. De Zanche, C. Barmet, J. A. Nordmeyer-Massner, and K. P. Pruessmann, *Magnetic Resonance in Medicine* **60**, 176 (2008).
- [3] J. Kitching, S. Knappe, and E. A. Donley, *IEEE Sensors Journal* **11**, 1749 (2011).
- [4] M. Jiang, W. Xu, Q. Li, Z. Wu, D. Suter, and X. Peng, *Advanced Quantum Technologies* **3**, 2000078 (2020).
- [5] M. Brownnutt, M. Kumph, P. Rabl, and R. Blatt, *Rev. Mod. Phys.* **87**, 1419 (2015).
- [6] K. A. Gilmore, M. Affolter, R. J. Lewis-Swan, D. Barberena, E. Jordan, A. M. Rey, and J. J. Bollinger, *Science* **373**, 673 (2021).
- [7] H. Fan, S. Kumar, J. Sedlacek, H. Kuebler, S. Karimkashi, and J. P. Shaffer, *Journal of Physics B: Atomic, Molecular and Optical Physics* **48**, 202001 (2015).
- [8] R. C. Jaklevic, J. Lambe, J. E. Mercereau, and A. H. Silver, *Phys. Rev.* **140**, A1628 (1965).
- [9] M. Hatridge, R. Vijay, D. H. Slichter, J. Clarke, and I. Siddiqi, *Phys. Rev. B* **83**, 134501 (2011).
- [10] R. L. Fagaly, *Review of Scientific Instruments* **77**, 101101 (2006).
- [11] L. Rondin, J.-P. Tetienne, T. Hingant, J.-F. Roch, P. Maletinsky, and V. Jacques, *Reports on Progress in Physics* **77**, 056503 (2014).
- [12] J. F. Barry, J. M. Schloss, E. Bauch, M. J. Turner, C. A. Hart, L. M. Pham, and R. L. Walsworth, *Rev. Mod. Phys.* **92**, 015004 (2020).
- [13] D. Suter and F. Jelezko, *Progress in Nuclear Magnetic Resonance Spectroscopy* **98-99**, 50 (2017).
- [14] R. Schirhagl, K. Chang, M. Loretz, and C. L. Degen, *Annual Review of Physical Chemistry* **65**, 83 (2014).
- [15] M. A. Nielsen and I. L. Chuang, *Quantum Computation and Quantum Information* (Cambridge University Press, Cambridge, 2000).
- [16] J. Stolze and D. Suter, *Quantum Computing: A Short Course from Theory to Experiment* (Wiley-VCH, Berlin, 2nd edition, 2008).
- [17] A. Zwick, D. Suter, G. Kurizki, and G. A. Alvarez, *Phys. Rev. Applied* **14**, 024088 (2020).
- [18] D. Suter and G. A. Alvarez, *Rev. Mod. Phys.* **88**, 041001 (2016).
- [19] G. A. Alvarez and D. Suter, *Phys. Rev. Lett.* **107**, 230501 (2011).
- [20] A. M. Souza, G. A. Alvarez, and D. Suter, *Phys. Rev. Lett.* **106**, 240501 (2011).
- [21] A. M. Souza, G. A. Alvarez, and D. Suter, *Phil. Trans. R. Soc. A* **370**, 4748 (2012).
- [22] G. Balasubramanian, P. Neumann, D. Twitchen, M. Markham, R. Kolesov, N. Mizuochi, J. Isoya, J. Achard,

- J. Beck, J. Tissler, et al., *Nature Materials* **8**, 383 (2009).
- [23] V. K. Kavatamane, D. Duan, S. r. Arumugam, N. Raatz, S. Pezzagna, J. Meijer, and G. Balasubramanian, *New Journal of Physics* **21** 103036 (2019).
- [24] T. Unden, P. Balasubramanian, D. Louzon, Y. Vinkler, M. B. Plenio, M. Markham, D. Twitchen, A. Stacey, I. Lovchinsky, A. O. Sushkov, et al., *Phys. Rev. Lett.* **116**, 230502 (2016).
- [25] J. Zhang, R. Laflamme, and D. Suter, *Phys. Rev. Lett.* **109**, 100503 (2012).
- [26] S. Zaiser, T. Rendler, I. Jakobi, T. Wolf, S.-Y. Lee, S. Wagner, V. Bergholm, T. Schulte-Herbrueggen, P. Neumann, and J. Wrachtrup, *Nature Communications* **7**, 12279 (2016).
- [27] X. Peng, D. Suter, and D. A. Lidar, *Journal of Physics B: Atomic, Molecular and Optical Physics* **44**, 154003 (2011).
- [28] J. H. Shim, I. Niemeyer, J. Zhang, and D. Suter, *Phys. Rev. A* **87**, 012301 (2013).
- [29] M. Lovric, P. Glasenapp, D. Suter, B. Tumino, A. Ferrier, P. Goldner, M. Sabooni, L. Rippe, and S. Kroell, *Phys. Rev. B* **84**, 104417 (2011).
- [30] M. Lovric, D. Suter, A. Ferrier, and P. Goldner, *Phys. Rev. Lett.* **111**, 020503 (2013).
- [31] M. H. Abobeih, J. Randall, C. E. Bradley, H. P. Bartling, M. A. Bakker, M. J. Degen, M. Markham, D. J. Twitchen, and T. H. Taminiau, *Nature* **576**, 411 (2019).
- [32] Y. Wu, F. Jelezko, M. B. Plenio, and T. Weil, *Angewandte Chemie International Edition* **55**, 6586 (2016).
- [33] M. Loretz, T. Roskopf, and C. L. Degen, *Phys. Rev. Lett.* **110**, 017602 (2013).
- [34] G. Wang, Y.-X. Liu, Y. Zhu, and P. Cappellaro, *Nano Letters* **21**, 5143 (2021).
- [35] P. Wang, Z. Yuan, P. Huang, X. Rong, M. Wang, X. Xu, C. Duan, C. Ju, F. Shi, and J. Du, *Nature Communications* **6**, 6631 (2015).
- [36] J. M. Schloss, J. F. Barry, M. J. Turner, and R. L. Walsworth, *Phys. Rev. Applied* **10**, 034044 (2018).
- [37] Y.-X. Liu, A. Ajoy, and P. Cappellaro, *Phys. Rev. Lett.* **122**, 100501 (2019).
- [38] X.-D. Chen, F.-W. Sun, C.-L. Zou, J.-M. Cui, L.-M. Zhou, and G.-C. Guo, *EPL (Europhysics Letters)* **101**, 67003 (2013).
- [39] G. Balasubramanian, I. Chan, R. Kolesov, M. Al-Hmoud, J. Tisler, C. Shin, C. Kim, A. Wojcik, P. R. Hemmer, A. Krueger, et al., *Nature* **455**, 648 (2008).
- [40] Z. Wang, F. Kong, P. Zhao, Z. Huang, P. Yu, Y. Wang, F. Shi, and J. Du, arXiv:2206.08533 [quant-ph] (2022).
- [41] T. Teraji, T. Taniguchi, S. Koizumi, Y. Koide, and J. Isoya, *Applied Physics Express* **6**, 055601 (2013).
- [42] J. Zhang, J. H. Shim, I. Niemeyer, T. Taniguchi, T. Teraji, H. Abe, S. Onoda, T. Yamamoto, T. Ohshima, J. Isoya, et al., *Phys. Rev. Lett.* **110**, 240501 (2013).
- [43] K. D. Jahnke, B. Naydenov, T. Teraji, S. Koizumi, T. Umeda, J. Isoya, and F. Jelezko, *Applied Physics Letters* **101**, 012405 (2012).
- [44] M. Hirose and P. Cappellaro, *Nature* **532**, 77 (2016).
- [45] F. Bloch and A. Siegert, *Phys. Rev.* **57**, 522 (1940).
- [46] J. Zhang, S. Saha, and D. Suter, *Phys. Rev. A* **98**, 052354 (2018).
- [47] A. P. Saiko, S. A. Markevich, and R. Fedaruk, *JETP Letters* **110**, 441 (2019).
- [48] The specific frequency was chosen to be sufficiently far from the resonance frequency of the NMR transitions, in order to avoid effects that are not related to the sensing via the electron spin.
- [49] T. Gullion, D. B. Baker, and M. S. Conradi, *Journal of Magnetic Resonance* (1969) **89**, 479 (1990).